

Low Frequency Radio Images of the Galaxy Cluster Abell 2256

H.T. Intema¹, R.J. van Weeren¹, H.J.A. Röttgering¹, D.V. Lal^{2,3}, and I.A.G. Snellen¹

¹ Leiden Observatory, Leiden University, P.O.Box 9513, NL-2300 RA, Leiden, The Netherlands

² National Centre for Radio Astrophysics, University of Pune, India

³ Max-Planck-Institut für Radioastronomie, Bonn, Germany

Received ... / Accepted ...

Abstract

The galaxy cluster Abell 2256 is a prime target for a study at low radio frequencies, because of the ultra-steep radio spectra of several features within the cluster, like the halo, relic and a strange 'source F' region. We present the results of high resolution GMRT observations at 153 and 325 MHz, and low-resolution WSRT LFFE observations at 8 frequencies within the range 115–165 MHz. In the low resolution maps, we make significant detections of both the central radio and the peripheral radio relic. We confirm the flattening of the spectral index of the relic towards the relic edge. Comparison of the total intensity and spectral index maps at this resolution with higher frequency observations suggest that the spectral index of the halo emission between 140 MHz and 1.4 GHz flattens from ~ -2 in the center to $\gtrsim -1.4$ towards the southern and eastern boundaries. We use the high resolution maps to study two confused regions within the cluster. The complex ultra-steep spectrum source F at the eastern cluster boundary probably consists of two AGN, of which one ceased activity. The brightest region (F2) fits the profile of a radio 'phoenix', old AGN plasma whose synchrotron emission was revived by shock compression. Near the cluster center we detect a long, steep-spectrum extension of a previously detected head-tail galaxy (source A) with a projected bend angle of ~ 80 degrees. In the same region we find a steep-spectrum region that may be a radio phoenix as well. These observations support a recent cluster merger scenario, in which disturbances in the ICM strongly influence the appearance of (previously) active radio galaxies.

1. Introduction

Diffuse synchrotron radio emission from galaxy cluster halos, relics and radio tails provides a unique diagnostic for studying the magnetic field (e.g. Feretti & Johnson-Hollitt 2004), plasma distribution and gas motion within clusters of galaxies. Galaxy clusters containing radio halos appear to have large X-ray luminosities and galaxy velocity dispersions (e.g. Hanisch 1982). These characteristics of dynamic activity are to be expected if the clusters are composed of merging sub-clusters, as predicted by some cluster evolution models (Kempner and Sarazin 2001 and references therein). A merger scenario is supported by the presence of highly polarized, megaparsec-scale relic structures at the periphery of some X-ray clusters (e.g., Röttgering et al 1997; Brentjens and de Bruyn 2004), which is thought to consist of fossil plasma that is revived by merger shocks (e.g., Enßlin & Gopal-Krishna 2001). Also the presence of head-tail galaxies in clusters is found to indicate a non-relaxed cluster state (Klamer, Subrahmanyan & Hunstead 2004). Their positions correlate with regions of enhanced X-ray emission and galaxy density (Mao et al. 2009).

Abell 2256 (A2256 from here on) is a rich nearby galaxy cluster at a mean redshift of $z = 0.0583$ (Miller, Owen & Hill 2003) that contains a radio halo, relic and several head-tail sources (Bridle et al. 1979; Röttgering 1994; Clarke &

Enßlin 2006; Brentjens 2008). The cluster contains a diffuse X-ray source, consisting of three substructures (Briel et al. 1991; Sun et al. 2002), that roughly coincides with the radio halo. The radial velocity distribution of galaxies has a large dispersion ($> 1200 \text{ km s}^{-1}$; Faber & Dressler 1977; Miller, Owen & Hill 2003) and seems to consist of three distinct groups (e.g., Berrington, Luger & Cohn 2002) based on position and velocity. This combined observational evidence has led to the conclusion that A2256 is currently undergoing a cluster merger.

Detailed studies of merging clusters like A2256 are essential to understand the formation of the largest structures in the Universe. Cluster radio emission usually has an ultra-steep radio spectrum (USS; $S_\nu \propto \nu^\alpha$ with $\alpha < -1$), which generally indicates the radiating electrons are old and can provide fossil records of the cluster history (e.g. Miley 1980). A study at low ($\lesssim 300 \text{ MHz}$) radio frequencies has the natural benefit of an increased relative brightness of USS sources and provides a view on aged synchrotron sources, complementary to the more recent radio activity as seen at higher ($\gtrsim 1 \text{ GHz}$) frequencies.

The effectiveness of low frequency observations has been limited for four main reasons: (i) the low resolution, (ii) sidelobe confusion from bright outlier sources, (iii) the ionosphere-induced phase distortions, and (iv) man-made radio frequency interference (RFI). The construction of larger and/or more sensitive low-frequency arrays (e.g., the

WSRT¹ at 115–165 and 325–377 MHz, the VLA² at 74 and 327 MHz and the GMRT³ at 153, 235 and 325 MHz), combined with the recent development of more advanced data reduction and imaging algorithms, has yielded significant improvements in the quality of low frequency radio maps.

In this paper we present deep continuum observations of A2256 with the GMRT at 153 and 325 MHz, as well as WSRT LFFE⁴ observations between 115–165 MHz. The compact WSRT has a rather low resolution ($\gtrsim 2'$), but is very sensitive to large-scale ($\gtrsim 1$ degree) emission from the halo and relic regions. The complementary high resolution observations with GMRT ($\sim 25''$ and $\sim 15''$ at 153 and 325 MHz, respectively) allow for a detailed study of compact emission regions that have been noted for their entangled or complex morphologies, like the region containing sources A & B and the source F region (e.g., Bridle et al. 1979; Röttgering et al. 1994).

In Section 2, we give a description of the observations and data reduction. In Section 3, we present and analyze the resulting images, followed by a discussion in Section 4. A summary is presented in Section 5. Throughout this paper, source positions are given in epoch J2000 coordinates. We adopt a flat, Λ -dominated cosmology with $\Omega_M = 0.27$, $\Omega_\Lambda = 0.73$ and $H_0 = 100 \text{ km s}^{-1} \text{ Mpc}^{-1}$ with $h = 0.71$ (Komatsu et al. 2009). For a mean redshift for A2256 of 0.0583 (Miller, Owen & Hill 2003), the conversion between angular size and proper size is $67 \text{ kpc arcmin}^{-1}$, or $4.0 \text{ Mpc degree}^{-1}$.

2. Observations and Data Reduction

In this section, we describe the observations and data reduction of the GMRT 153 MHz and WSRT 115–165 MHz observations on the A2256 field (pointing center at $17^{\text{h}}03^{\text{m}}09.06^{\text{s}}$, $+78^\circ39'59.7''$). The observations and reduction of the GMRT 325 MHz data are described separately in van Weeren et al. (*in preparation*).

2.1. GMRT 153 MHz

A2256 was observed with the GMRT in a 6 MHz wide protected radio band, centered at 153 MHz (see Table 1 for more information). Combining 14 antennas in a central square kilometer and 16 antennas in an extended Y-shape up to 35 km baselines makes GMRT sensitive to a wide range of spatial scales. The field-of-view (FoV) diameter at 153 MHz, defined by the half-power beam width (HPBW), is 3.1 degrees, while the resolution is typically 20–25''. Although the observing band is protected, significant man-made radio frequency interference (RFI) is present within the band at all times. The low-frequency observations are further complicated by ionospheric phase rotations that vary with time and viewing direction, and are relatively strong at the low latitude location of GMRT relatively near the geomagnetic equator. Observing in spectral channel mode with short integration times allows for more selective excision of detectable RFI, allows for more accurate (ionospheric phase) calibration, and reduces band-

width and time-averaging smearing during wide-field imaging.

Data reduction was done using the Astronomical Image Processing Software (AIPS; e.g. Bridle & Greisen 1994) package, developed by the National Radio Astronomy Observatory (NRAO). Furthermore, we used the (recent) SPAM software package (Intema et al. 2009a, 2009b) to incorporate direction-dependent ionospheric phase calibration. SPAM utilizes AIPS tasks and files through the ParselTongue interface (Kettenis et al. 2006), while providing high-level tasks for basic calibration & imaging and for calibration of direction-dependent ionospheric phase errors. For the latter, SPAM measures the antenna-based, direction-dependent phase errors by peeling bright sources in the FoV (Noordam 2004), separates instrumental from ionospheric phase contributions, combines the ionospheric phases into a consistent phase screen model, and predicts the ionospheric phase corrections in arbitrary viewing directions while imaging the FoV.

The GMRT observation included 20 minutes on 3C 48 at the end of the observing run. Following the SPAM recipe for data reduction, we used 3C 48 for flux, bandpass and instrumental phase calibration. Initial flagging of all visibility data included removal of dead and malfunctioning antennas and baselines, systematic removal of the first 30 seconds of each observing time blocks due to potential system instabilities, and manual and semi-automated flagging of channels and time ranges on individual baselines, based on excessive ($\gtrsim 5$ times the RMS) visibility amplitudes. An initial phase calibration was performed on 3C 48 against a 62.71 Jy point source model (Perley-Taylor 1999.2 scale⁵) using a small, relatively RFI-free channel range (unless stated otherwise, phase-only calibrations are all performed on the highest possible time resolution = 16.8 seconds). A single time-constant bandpass calibration on 3C 48, normalized to the same channel range, was performed while temporarily applying the phase calibration. After excision of 48 noisy channels at both edges of the bandpass, spectral resolution was reduced by averaging every 4 channels into 20 channels of 0.25 MHz. This was followed by more flagging and a single, unconstrained flux calibration to the point source model while temporarily applying both phase and bandpass calibrations. The RR and LL polarizations were combined into stokes I while applying the bandpass and flux calibration, which was followed by a phase calibration using the full bandwidth. The time-varying calibration phase corrections were filtered to estimate the (presumed) constant instrumental phase offsets, by iterative fitting of time-variant, spatial phase gradients (Cotton et al. 2004; Intema et al. 2009a).

The flux, bandpass and instrumental phase calibrations were transferred to the A2256 field data, which was flagged and combined in the same way as the 3C 48 data. This data was phase calibrated against a 35 point source model, derived from power-law extrapolation of NVSS and WENSS source fluxes and corrected for primary beam attenuation. This was followed by wide-field imaging of the primary beam area (Table 2), followed by 3 rounds of phase-only self-calibration & imaging. After each self-calibration round, the source model was temporarily subtracted from the visibility data, followed by flagging of excessive resid-

¹ Westerbork Synthesis Radio Telescope

² Very Large Array

³ Giant Metrewave Radio Telescope

⁴ Low Frequency Front End

⁵ Defined in the ‘VLA Calibrator Manual’, available online at <http://www.vla.nrao.edu/astro/calib/manual/baars.html>

Observation	Date(s)	Int. Time [sec]	Total Time [hours]	Bandwidth [MHz]	Ch. Width [kHz]	Pol'ns
GMRT 153 MHz	June 5, 2005	16.8	8.2	8 ^a	62.5	RR,LL
GMRT 325 MHz	May 25&26, 2008	16.8	9.5	2 × 16	125	RR,LL
WSRT 115–165 MHz ^b :						
36 m spacing	Dec. 1, 2004	10.0	10.0	8 × 2.5	1.95	XX,YY,XY,YX
48 m spacing	Dec. 4&6, 2004	10.0	10.5	8 × 2.5	1.95	XX,YY,XY,YX
60 m spacing	Dec. 8&10, 2004	10.0	11.3	8 × 2.5	1.95	XX,YY,XY,YX
72 m spacing	Dec. 11, 2004	10.0	10.8	8 × 2.5	1.95	XX,YY,XY,YX
84 m spacing	Dec. 15, 2004	10.0	10.8	8 × 2.5	1.95	XX,YY,XY,YX
96 m spacing	Dec. 18, 2004	10.0	10.7	8 × 2.5	1.95	XX,YY,XY,YX

^a Effectively reduced to 5–6 MHz by antenna-based bandpass filters.

^b Observations consist of 6 array configurations, or spacings.

Table 1: Overview of observations on the A2256 field.

Field diameter	4.9° ^a
Pixel size	4.2''
Weighting	robust 0.5 ^b
Wide-field imaging	polyhedron (facet-based) ^c
Number of initial facets	109
Facet diameter	0.60°
Facet separation	0.50°
Deconvolution	Cotton-Schwab CLEAN ^d
CLEAN box threshold ^e	5σ
CLEAN depth ^e	2σ
Restoring beam	22.1'' × 16.7'' (PA 39.5°)

^a We map more than twice the HPBW diameter to allow for deconvolution of nearby bright sources.

^b Briggs 1995

^c Perley 1989; Cornwell & Perley 1992

^d Schwab 1984; Cotton 1999;
Cornwell, Braun & Briggs 1999

^e σ is the background RMS, measured in the central part of the image.

Table 2: Overview of GMRT imaging parameters.

Calibration cycles	2
Peeled sources ^a	20
Number of added facets	20
Layer heights (weights)	100 km (0.25) 200 km (0.50) 400 km (0.25)
Parameter γ ^b	5 / 3
Model parameters	20
Model fit phase RMS ^{a,c}	22.2° ± 4.2°
Peeling corrections applied	yes
Phase drift estimates applied	yes
Reference catalog	NVSS ^d

^a Specified for the final (second) calibration cycle only.

^b Adopted power-law slope of the overall phase structure function.

^c After rejection of excessive model fit errors > 40 degrees.

^d Condon et al. 1994, 1998

Table 3: Overview of the SPAM processing parameters. For more information on the meaning of the parameters we refer to Intema et al. (2009a; 2009b).

ual visibility amplitudes. After subtracting the last source model, the visibility data was imaged at the positions of potentially interfering bright outlier sources (nearby bright and far-away extremely bright sources like the Sun, Cas A, Cyg A, etc.), but no significant flux was detected. Self-calibration was followed by two additional rounds of SPAM calibration and imaging (see Table 3). In this process we lost ∼ 50 percent of the data due to excessive ionospheric model fit errors for which we were unable to correct. Still, using the remaining data significantly reduced the image artefacts near bright sources, resulting in a final background RMS of 2.1 mJy beam^{−1}, measured over the inner half of the primary beam area.

To enable the detection of the known diffuse radio sources in A2256, we have attempted to conserve as many short baselines as possible during flagging, although the RFI was particularly severe on these baselines. For the final image, we have attempted to boost the contrast of the diffuse emission by applying different weighting schemes (natural weighting, gaussian tapering of the UV-plane), but this only resulted in enhancing large-scale ripples in the image

background, therefore these attempts were abandoned. As a result, the sensitivity for large-scale emission is compromised, but we retain a good signal on smaller, more compact emission regions.

The final image was corrected for primary beam attenuation with a circular beam model⁶

$$A(\theta, \nu) = 1 - 4.04 \cdot 10^{-3} (\theta\nu)^2 + 76.2 \cdot 10^{-7} (\theta\nu)^4 - 68.8 \cdot 10^{-3} (\theta\nu)^6 + 22.03 \cdot 10^{-3} (\theta\nu)^8, \quad (1)$$

where θ is the angular distance from the pointing center in arcminutes and ν the observing frequency in GHz.

2.2. WSRT 115–165 MHz

A2256 was observed with the WSRT in eight radio bands in the range 115–165 MHz (Table 4). The eight bands were po-

⁶ From the GMRT User Manual

Field diameter	15.0°
Pixel size	40'' – 50'' ^a
Weighting	robust 0.
Wide-field imaging	polyhedron (facet-based)
Number of facets	200
Facet diameter	85' – 107'
Facet separation	81'
Deconvolution	Cotton-Schwab CLEAN
CLEAN box threshold	? σ
CLEAN depth	? σ
Restoring beam	circular 2.1 – 2.9' ^a

^a See Table 4 for setting per band.

Table 5: Overview of WSRT imaging parameters. See Table 2 for more info.

sitioned in frequency to minimize RFI within the observing bands. To improve UV-coverage and sensitivity, and suppress grating lobes due to the regular 144 meter spacings of the 10 fixed antennas, the A2256 field was observed for 12 hours (full synthesis) in each of six ‘traditional’ configurations⁷ of the four movable antennas (Table 1).

Because of limitations in the data reduction software to simultaneously image and deconvolve the large LFFE frequency span (e.g., varying primary beam shapes, resolutions and spectral indices), each of the eight bands was processed independently. Data reduction was performed using the AIPS package, which started with initial flagging of RFI and bad data (similar to Section 2.1), excising between 10–40 percent of the data per band under varying conditions over time and frequency. Each observing day (i.e., each spacing) included 15 minute calibrator observations of 3C 295 and 3C 48, which were used to determine the time-constant, normalized bandpass calibration. After applying the bandpass calibration, more flagging was done, including 17 frequency channels at the band’s edges. Flux calibration was postponed to a later stage, because of uncertainties in the gain amplitude determination from a non-isolated calibrator in the large FoV.

To monitor ionospheric activity per observing day, both 3C 295 and 3C 48 were phase calibrated on the visibility time resolution against point source models. We hand-picked a visibility data subset of high quality (little RFI and stable ionospheric phases) for one frequency band – spacing combination (‘subset’ from here on) to generate a target field model, namely the 139.25 MHz data at the 36 meter spacing. For this subset, the phase corrections from the calibrators were transferred to the target field. The target field was imaged over twice the primary beam radius (Table 5) to facilitate removal of nearby bright outliers. Next, the data was self-calibrated & imaged for three rounds, of which the final round also included amplitude calibration.

All other subsets were phase calibrated against the target field model derived above, followed by imaging and one round of (amplitude & phase) self-calibration & imaging. After subtracting the appropriate target field model from each visibility subset (including nearby outliers), the visibility data was imaged at the positions of five extremely bright outlier sources, namely the Sun, Cas A, Cyg A, Vir A and Tau A. Because the apparent fluxes of these

sources were significant, each of these sources was peeled (Noordam 2004). Before adding back the target field source model (excluding nearby outliers), all residual visibility data was re-inspected for RFI and flagged where needed. The visibility data of the different spacings was combined per band into 8 large data sets. The data volume was reduced through spectral and temporal averaging of each 3 channels and 2 time stamps, respectively, resulting in 5.85 KHz channels and a 20 second visibility time resolution. Each band was imaged, followed by one round of (amplitude & phase) self-calibration & imaging.

Each image was corrected for primary beam attenuation with a circular beam model⁸

$$A(\theta, \nu) = \cos^6(1.1 \theta \nu), \quad (2)$$

where θ is the angular distance from the pointing center in arcminutes and ν the observing frequency in GHz. For the absolute flux calibration we used 5 bright point sources in the center of the FoV for which flux measurements are available in the 74 MHz VLSS, 151 MHz 6C, 327 MHz WENSS and 1.4 GHz NVSS catalogs (Cohen et al 2007; Hales, Baldwin, & Warner 1988; Rengelink et al. 1997; Condon et al. 1994, 1998) and are present in the GMRT 153 MHz image (Section 2.1). Fluxes of these sources were measured in the GMRT 153 MHz band and WSRT LFFE bands through gaussian fitting in the images. The catalog fluxes (including GMRT 153 MHz) were fitted per source with a power-law spectrum, allowing for a possible turnover at low frequencies (Figure 1). From these fits, we determined the amplitude correction factors per WSRT band, averaged over the 5 sources, and apply these directly to the images. We adopt an absolute flux calibration uncertainty of 10 percent, but anticipate that the relative flux error between WSRT bands is much smaller.

The background RMS of all WSRT images (Table 4) appears to be limited by systematic rather than noise-like fluctuations, which we interpret to be a combination of ionospheric phase errors, residual RFI and other calibration errors. We have not attempted direction-dependent ionospheric phase calibration, because the one-dimensional geometry of WSRT complicates ionospheric modeling. Because of the limited size of the WSRT array, it is likely to operate in the ionospheric calibration regime where sources suffer from apparent differential movement without any source deformation (regime 3 in Lonsdale 2005). The resulting ionospheric smearing over 12 hour observations is expected to cause a minor ($\lesssim 2$ percent) broadening of the 2' – 3' beam.

3. Results

3.1. Total Intensity Maps

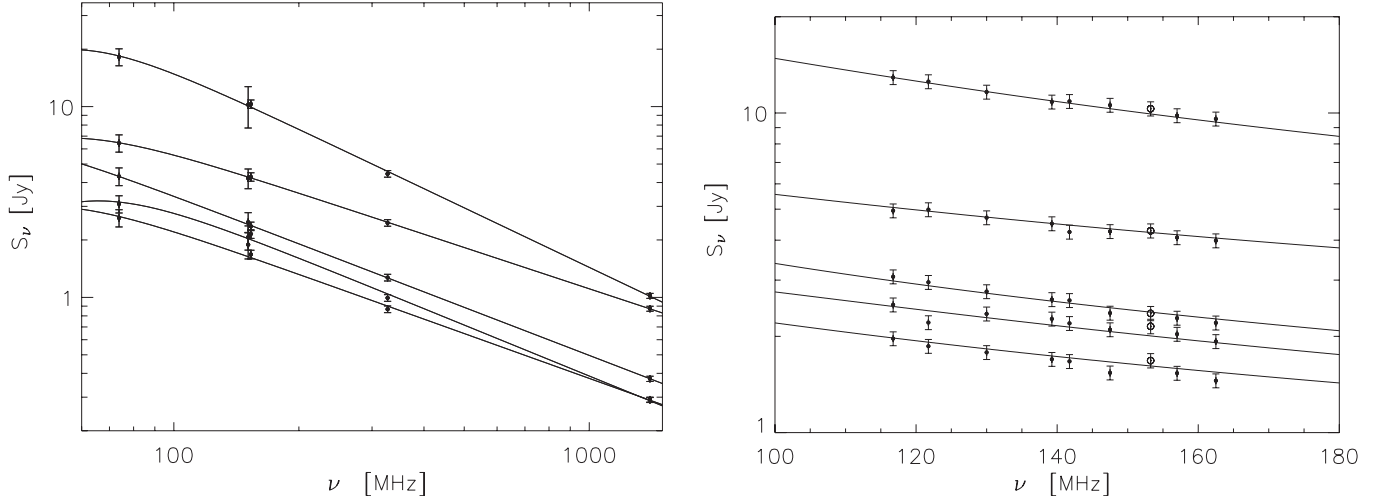
In Figures 2 and 3 we present the total intensity maps from the GMRT 153 and 325 MHz observations. We used the deeper 325 MHz image ($0.20 \text{ mJy beam}^{-1}$ background RMS) to mark various sources as identified by Bridle et al. (1979) and Röttgering et al. (1994). This map clearly shows several radio features for which this cluster is best known: the head-tail sources A, B, C and I, the steep spectrum source F consisting of several components, the large relic area surrounding sources G and H, and traces of the

⁷ See the WSRT Guide to Observations

⁸ From the WSRT Guide to Observations

Frequency	HPBW	Resolution	Pixel Size	Background RMS
116.75 MHz	15.5°	2.9'	50''	14.6 mJy beam ⁻¹
121.75 MHz	14.8°	2.8'	50''	14.3 mJy beam ⁻¹
130.00 MHz	13.9°	2.6'	50''	7.2 mJy beam ⁻¹
139.25 MHz	13.0°	2.45'	40''	7.1 mJy beam ⁻¹
141.75 MHz	12.7°	2.4'	40''	7.1 mJy beam ⁻¹
147.50 MHz	12.2°	2.3'	40''	6.1 mJy beam ⁻¹
157.00 MHz	11.5°	2.2'	40''	5.0 mJy beam ⁻¹
162.50 MHz	11.1°	2.1'	40''	6.0 mJy beam ⁻¹

Table 4: Overview of some WSRT LFFE observing characteristics.

Figure 1: Flux models and corrections for 5 bright point sources in the vicinity of A2256. *Left:* Fitted spectral models based against catalog flux measurements (filled dots) at 74, 151, 153, 327 and 1400 MHz for sources (top to bottom) 4C 79.17, 4C 79.16, 6C B165417.3+783341., 6C B171152.4+801023, and 6C B170753.6+775949. *Right:* Comparison of the WSRT LFFE corrected fluxes (filled dots) and GMRT 153 MHz flux (open dot) against the fitted spectral models.

diffuse halo centered approximately on source D. In the 153 MHz map, only parts of the relic area are detected due to poorer sensitivity and a loss of short baselines to RFI. There is no significant detection of halo emission. Sources with more compact emission, like sources A, B, C and F, are detected at significant levels, as well as several of the point-like sources farther out. We discuss the source complex A–B and source F in more detail in Sections 3.4 and 3.5.

The background structure of the final WSRT images due to residual calibration errors varies from band to band, resulting in a varying contrast on the diffuse emission regions in A2256. Most prominent are residual grating lobes. Instead of interpreting the results from ‘noisy’ individual bands, we combined them to reduce the effect of artefacts in individual maps. We excluded two bands (121.75 and 147.50 MHz), in which the image artefacts seem to have a severe effect on the emission of A2256. Because the image combination is a non-trivial operation considering the variation in spectral index across A2256 (e.g., Clarke & Enßlin 2006), we performed this operation after determination of the WSRT spectral index map over the A2256 area (Section 3.2). Convolving the remaining 6 bands to a common resolution of 2.9' and resampling to a common 50'' pixel grid was followed by combining into a single

~140 MHz map using the mean spectral index of -1.65 over the 115–165 MHz range for appropriate flux scaling. The resulting image was resampled to the 2.2'' grid of the 325 MHz GMRT observations, using a 4 pixel width interpolation kernel to smooth the image across pixel boundaries (see Figure 3).

The peaks in the emission coincide with the source combination A–C, the source F and the relic source G, while smaller peaks in the south coincide with sources O and L. The extended relic area is detected at high S/N, while the halo emission is clearly detected in the area between sources D and O. The 140 MHz halo shape roughly agrees with the halo detections at 350 MHz (Brentjens 2008) and 1.4 GHz (Clarke & Enßlin 2006), but does not continue as far southward (beyond sources O and L) as is seen in the other two maps.

There are two interesting extensions outside the diffuse halo & relic regions, one extending westward of the tail end of source C ($17^{\text{h}}00^{\text{m}}$, $+78^{\circ}43'$) and one extending eastward from the halo area below source F ($17^{\text{h}}08^{\text{m}}$, $+78^{\circ}34'$), that coincide with two filamentary radio sources in the GMRT 325 MHz map. These sources are also visible in the 350 MHz map by Brentjens (2008). The western extension also coincides with a very steep spectrum region in the WSRT

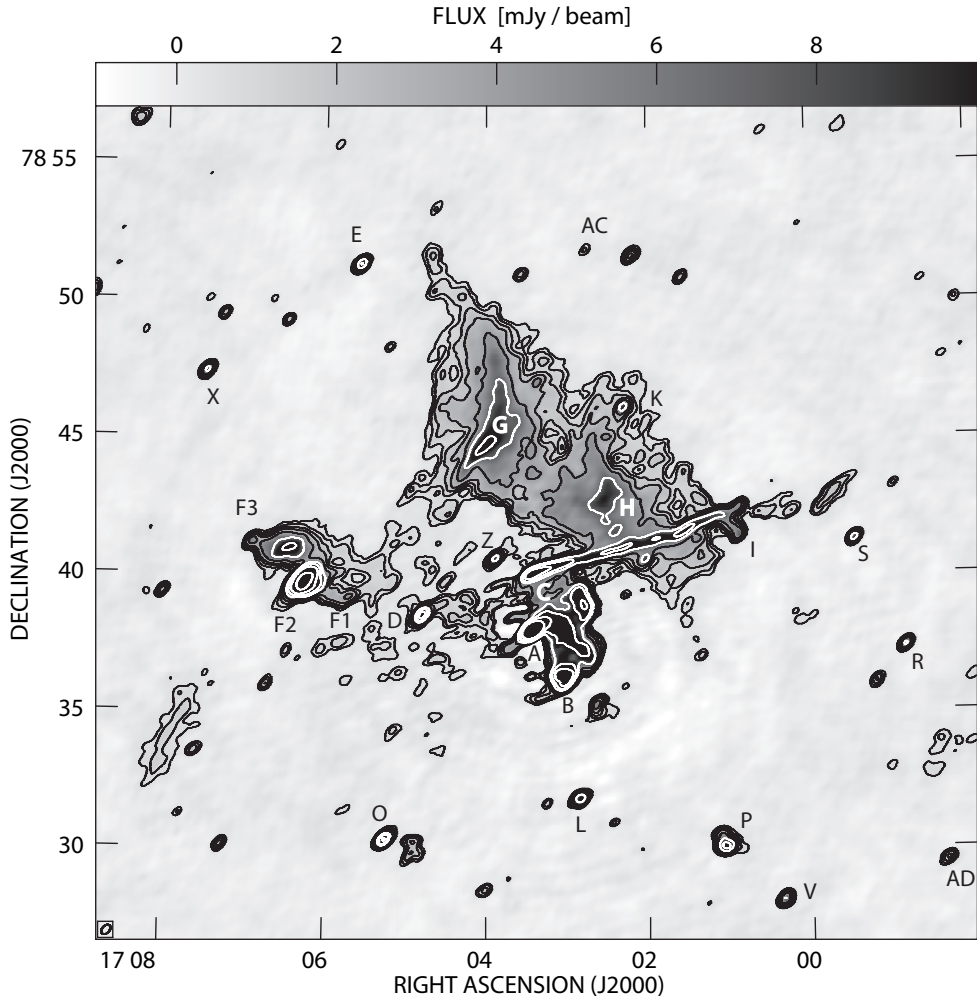


Figure 2: Greyscale plot of A2256 at 325 MHz as observed with GMRT. The background RMS is $0.20 \text{ mJy beam}^{-1}$. The synthesized beam width of $24'' \times 16''$ is depicted in the bottom-left corner. Contours are drawn at $[3, 5, 8, 12, 20, 36, 60, 100, 200] \times$ the background RMS. The capital letters are source labels as defined by Bridle et al. (1979) and Röttgering et al. (1994).

spectral index map (Section 3.2). Van Weeren et al. (*in preparation*) discusses these two regions in further detail.

3.2. Spectral Index Maps

In Figure 4 we present two spectral index maps of the full A2256 region. The low resolution spectral index map was created from the 6 WSRT bands, by fitting a power-law to the (band-dependent) values of each common ($50''$) pixel, and blanking those pixels that had less than 4 values above 3 times the background RMS. Like with the total intensity map, the spectral index map was resampled to the GMRT 325 MHz pixel grid. Pixels within $\sim 50''$ of the edge of colored islands have a spectral index fit uncertainty of ~ 1 , which explains the presence of several green/blue noise blobs at the edge. Beyond, the uncertainty rapidly drops to 0.2–0.3 for typical regions and < 0.1 for peak regions. The uncertainty includes the effect of map noise in individual bands. UV-coverage has little effect on the spectral index accuracy, because even at the highest frequency the WSRT array is sensitive to spatial scales $\gtrsim 0.5$ degrees.

The high resolution spectral index map was created from the 153 and 325 MHz GMRT maps. Fitting gaussians to 10 common point sources in both images and comparing peak positions showed that the systematic astrometric offset between both maps was less than $2''$. Both images were convolved to a circular $24''$ beamsize, after which the 153 MHz map was resampled to the $2.2''$ grid of the 325 MHz map. The spectral index was calculated per pixel, again only using pixels above 3 times the background RMS. Because of the better sensitivity of the 325 MHz map, the spectral index determinations are mainly limited by the 153 MHz pixels. In this case, the effects of UV coverage are important, because both at 153 and 325 MHz the GMRT resolves the large-scale emission. Convolution to the same resolution does help to create a better match in coverage in the outer UV-plane, but does little for matching the inner UV-plane where the large-scale sensitivity is defined. This means that the high resolution map is accurate in representing the changes in spectral index on smaller scales, but less accurate in determining the absolute spectral index in large-scale diffuse emission areas.

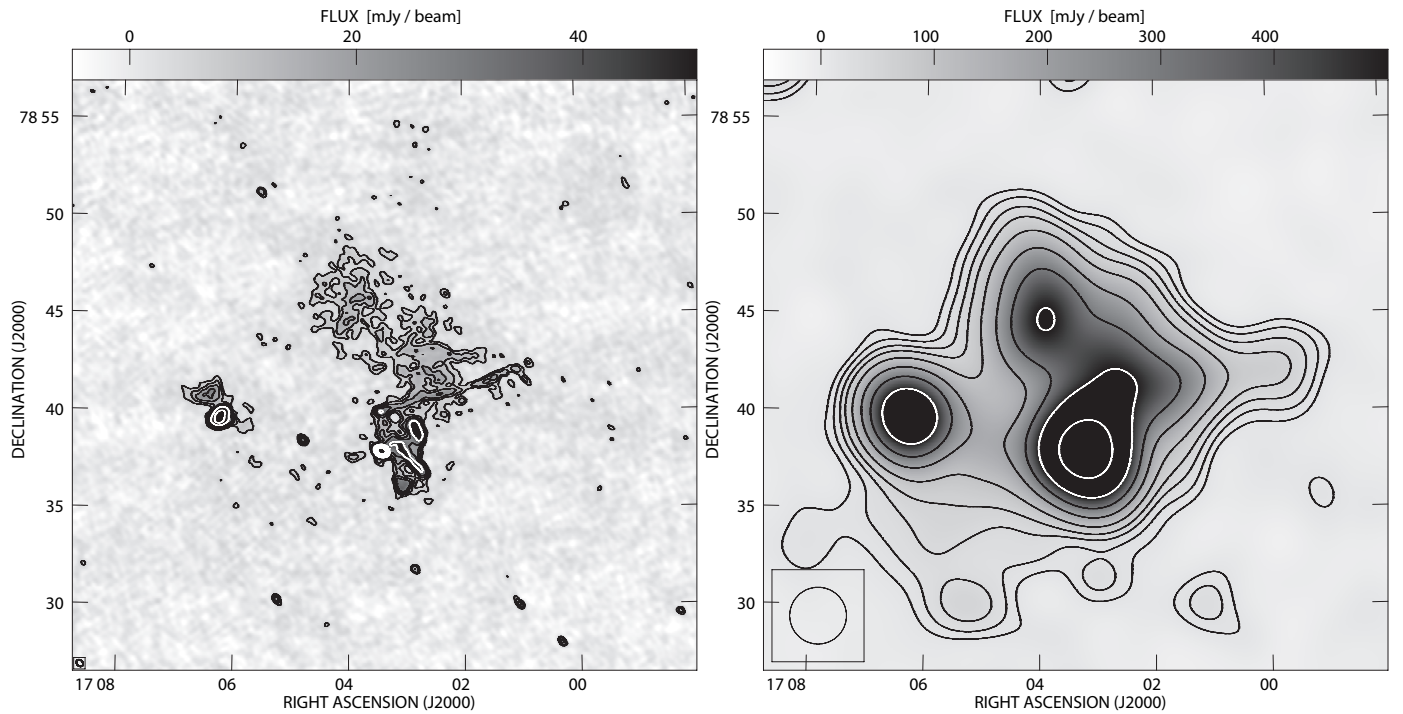


Figure 3: Greyscale plots of A2256. *Left:* Result of GMRT 153 MHz observations, yielding a synthesized beam width of $22.1'' \times 16.7''$ and a background RMS of $2.1 \text{ mJy beam}^{-1}$. *Right:* Combined WSRT map at an equivalent frequency of 140 MHz, with a circular beam width of $2.9'$ and a background RMS is $5.5 \text{ mJy beam}^{-1}$. Contours in both maps are drawn at $[3, 5, 8, 12, 20, 36, 60, 100, 200] \times$ the background RMS.

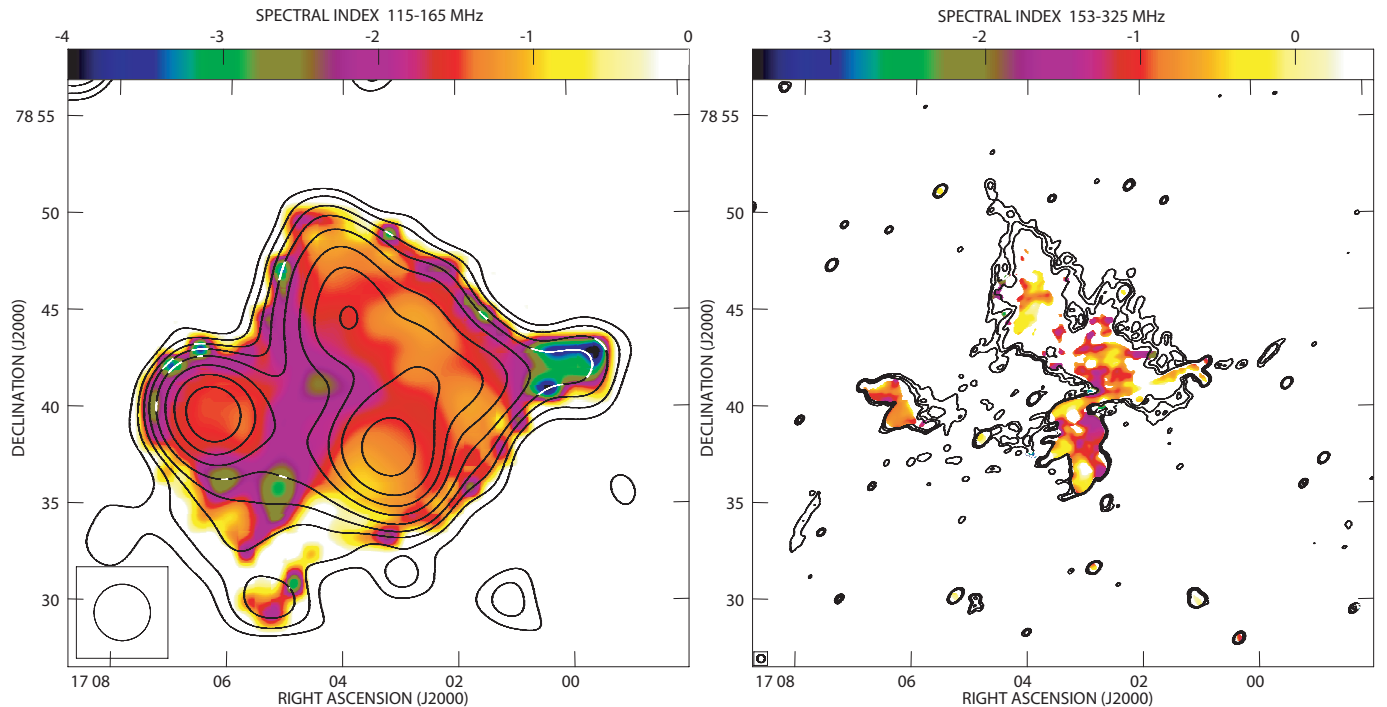


Figure 4: Spectral index maps of A2256. *Left:* Low resolution spectral index map, measured across 6 WSRT bands between 115–165 MHz. The overplotted contours are taken from the total intensity map in Figure 3. *Right:* High resolution spectral index map, measured between 153–325 MHz. The overplotted contours are 325 MHz total intensity contours (Figure 2) at $[5, 8, 12] \times$ the background RMS. Note that the spectral index color bar is shifted by 0.5 between both maps.

3.3. Large-scale Flux Distribution

In the low-resolution spectral index map (Figure 4) there is a certain degree of mixing of emission from different regions. The relic and halo regions are extended enough to have little contamination over substantial parts of their area. Away from sources A–C and the western extension, the relic area appears to have a rather uniform large-scale spectral index distribution. We identify two distinct transitions in the emission area, between the relic and the western extension and between the relic and the halo. These transitions coincide with relic boundaries as seen in the 325 MHz GMRT total intensity map and at higher frequency (e.g., Röttgering et al. 1994; Clarke et al. 2006). While keeping away from the noisy edge, we notice a steepening trend of the mean spectral index from north-west ($\alpha \approx -1$) to south-east ($\alpha \approx -1.5$). Due to the poor resolution, it is expected that part of the steepening is caused by the gradual transition towards the steeper halo emission. As the spectral steepening is measured within one of the higher total intensity contours, it is expected not to suffer from the apparent spectral steepening towards lower flux levels (like at the edge). The steepening trend is similar to that observed at 1.4 GHz by Clarke & Enßlin. (2006). The mean spectral index along a line running from NW to SE parallel to the relic edges, is -1.2 ± 0.1 . This is slightly steeper, but consistent within error margins, with the value of -1.0 ± 0.1 at 1.4 GHz. The spectral index map at 350 MHz by Brentjens (2008) shows much more variation across the relic, with no clear steepening trend.

Between sources A & B, source F and the relic region there is a relatively uncontaminated view on part of the halo emission. This region has a rather uniform spectral index of ~ -2 , clearly steeper than the emission from the relic and compact source regions. The spectral index map between 1.37–1.71 GHz by Clarke & Enßlin. (2006) also shows a significant steepening of the halo emission (possible < -3) as compared to other emission regions, although this result is stated to be possibly affected by UV-coverage. For the southern part of the halo we lack sensitivity for accurate spectral index determinations. Our spectral index measurement of the halo is similar to other low-frequency estimates of -1.9 between 22.25–81.5 MHz (Costain, Bridle & Feldman 1972) and -1.8 between 151–610 MHz (Bridle et al. 1979), although the latter estimate is uncertain because it is based on a resolved halo map at 610 MHz (Brentjens 2008).

We estimate the combined flux of all sources in the cluster by hand-drawing an outer contour around the continuous flux area in the low-resolution 140 MHz map (Figure 3) and summing the flux within. Repeating this process for more strict and more wide areas gave similar values, which we combined into a single estimate of 7.0 ± 0.9 Jy. This includes a ~ 10 percent uncertainty in the determination of the absolute flux scale. This estimate is consistent (within error margins) with the 151 MHz flux estimate of 8.1 ± 0.8 Jy by Masson & Mayer (1978; converted to the Perley & Taylor scale by Brentjens 2008), but less so with double-powerlaw model flux of 8.7 ± 0.4 Jy at 140 MHz by Brentjens (2008). As a check, we have measured the total flux of A2256 in the images of individual WSRT bands and find that the flux model $S_\nu = 7.0(\nu/140 \text{ MHz})^{-1.65}$ is a good representation of the individual measurements, where we have taken the mean frequency and mean spec-

tral index that were used for the construction of the total intensity map in Section 3.1.

From the radio halo maps at 350 MHz and 1.4 GHz we notice that the halo emission extends beyond our detection limit in the low-resolution spectral index map, therefore we miss a fraction of the total flux. From the noise levels of the 350 MHz and 1.4 GHz maps we derive that both are approximately equally sensitive for a spectral index of -1.4. We observe that the 1.4 GHz halo extends further eastward than the 350 MHz halo, which suggests that the spectral index flattens to > -1.4 in this region. The model radio spectrum of A2256 by Brentjens (2008) assumes a single mean spectral index of -1.61 ± 0.04 for the halo. This can be made consistent with the observations above when assuming that the spectral index varies across the halo, flattens considerably towards the southern and eastern edge, and assign total flux differences to limitations in sensitivity. We do note that the fitted model spectral index for the halo by Brentjens (2008) depends strongly on their estimated halo flux at 350 MHz and the estimate at 1.4 GHz by Clarke & Enßlin (2006), which may be affected by their estimates of invisible halo flux coincides with bright emission from relic and the more compact sources (A–D, F, etc.).

3.4. Sources A & B

The high resolution and smaller-scale sensitivity of the GMRT observations at 153 and 325 MHz allow for a detailed study of cluster regions with a complex emission structure. Here, we focus on the source complex A & B, and in the next section on complex source F.

Previous high resolution observations at 1.4 GHz and 2.7 GHz depict source A as a point-like source that coincides with an optical galaxy at redshift $z = 0.0586$ (Miller, Owen & Hill 2003), with an $30'' - 40''$ extending tail to the west (Bridle & Fomalont 1976; Röttgering et al. 1994; Miller, Owen & Hill 2003). At lower resolution, the 1.4 GHz and 330 MHz maps Röttgering et al. (1994) show that the tail extends further west and possibly bends southwards, but its appearance becomes confused with the tail extending from source B. Miller, Owen & Hill (2003) also detect an extension eastwards of the emission peak, which they identify as independent radio emission from the western nucleus of neighbouring galaxy NGC 6331. Deep, lower resolution images at 350 MHz (Brentjens 2008) and 1.4 GHz (Clarke & Enßlin 2006) show that the whole source A & B complex is embedded in diffuse emission from the halo. No apparent morphological relation exists between sources A & B and the diffuse relic area.

Previous high resolution observations of source B shows the classical morphology of a head-tail galaxy with a wide-angle tail (Röttgering et al. 1994), similar to NGC 1265 in the Perseus cluster (Miley 1973). From the core emission that coincides with an optical galaxy counterpart at $z = 0.0548$ (Miller, Owen & Hill 2003), two radio lobes emerge on the east- and west-side and bend northwards. The length of the brightest part of the head-tail is $40 - 50''$ along a north-south line, but fainter emission continues further north (see also Clarke & Enßlin 2006). In the lower resolution 1.4 GHz and 330 MHz maps from Röttgering et al. (1994) it appears that the tail emission continues northward beyond source A towards the extreme head-tail source C. Because of this apparent morphological connec-

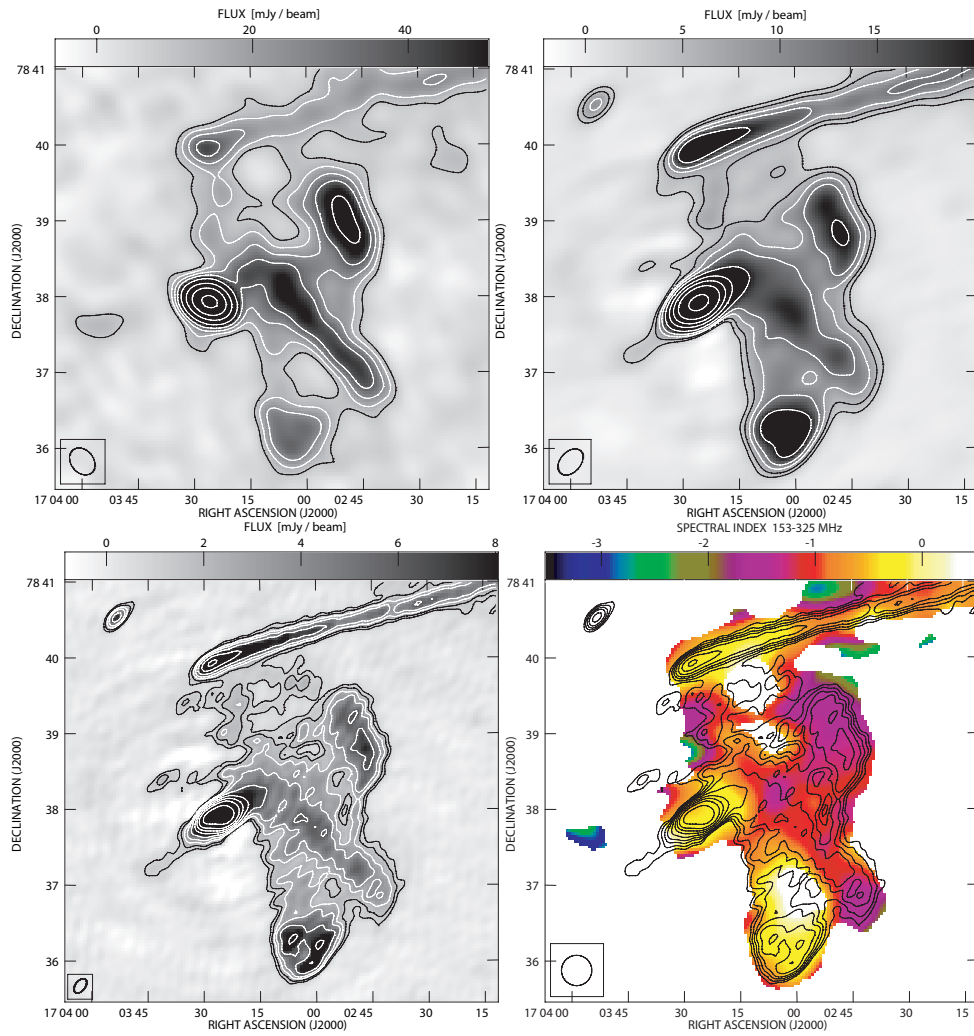


Figure 5: Detailed maps of the confused region of sources A & B in A2256. *Top Left:* Magnification of the GMRT 153 MHz map in Figure 3. Contours are drawn at $[5, 8, 12, 18, 30, 54, 90, 150, 300] \times$ the background RMS. *Top Right:* Magnification of the GMRT 325 MHz map in Figure 2. Contours are drawn at $[15, 25, 40, 60, 100, 180, 300, 500, 1000] \times$ the background RMS. *Bottom Left:* Uniform weighted map (instead of robust weighted) of the GMRT 325 MHz, yielding a beam width of $13.1'' \times 7.8''$ and a background RMS of $0.12 \mu\text{Jy beam}^{-1}$. Contours are drawn at $[7, 12, 20, 28, 50, 90, 150, 250, 500] \times$ the background RMS. *Bottom Right:* Spectral index map of the GMRT observations between 153–325 MHz map, convolved to a common beam width of $24'' \times 24''$. Contours are taken from the uniform weighted map.

tion, it seems unlikely that the apparent tail extension is halo emission.

We attempt to disentangle the emission seen in this area by assuming a minimal number of (previously) active galaxies involved. Figure 5 shows magnifications of the source A & B area from the two GMRT maps at 153 and 325 MHz, as well as a uniform-weighted map at 325 MHz to boost the resolution (which is not used for flux measurements). Similar to Section 3.3, we estimate the flux of the compact, bright regions of sources A and B at 153 and 325 MHz by drawing image contours around their core areas and summing the flux within. For source A, we find fluxes of 0.53 ± 0.02 Jy at 153 MHz and 0.41 ± 0.02 at 325 MHz, and for source B we find 0.15 ± 0.04 Jy at 153 MHz and 0.13 ± 0.01 at 325 MHz. The specified uncertainties do not include systematic uncertainties in the absolute flux scale.

In all GMRT maps there is a $\sim 2.5'$ (~ 170 kpc projected) tail of visible emission that runs from SW to NE,

which appears to connect to source A under a ~ 80 degree angle. The connection between this tail and source A is strengthened by the 1.4 and 2.7 GHz observations of source A (Bridle & Fomalont 1976; Röttgering et al. 1994; Miller, Owen & Hill 2003) in which the visible tail from source A overlaps with the low frequency tail and appears to have a bend in the direction of the low-frequency tail. For sake of convenience, we call this tail source A2. Bridle & Fomalont (1976) noticed a spectral steepening in westward direction, which they found to be consistent with a head-tail configuration. The emission from the long ($\sim 2'$) low-frequency source A2 is confused with emission that appears to originate from source B, except for a small length at the SW end of the tail. When considering the 153 MHz and uniform-weighted 325 MHz maps, the strongest emission originates from a rather well-confined $\sim 30''$ thin strip (≈ 35 kpc), therefore it seems reasonable to assume that source A2 is intrinsically narrow. The tail end has a signif-

icantly steeper spectrum (-1.6) than near source A (-0.3), which fits the typical profile of spectral steepening along a radio tail (e.g., Jaffe & Perola 1973). Ignoring the smallest variations, the spectral index along source A2 in the overlap region with source B is rather constant (-1 to -1.2). The measured total flux within the thin strip over the 2' tail length is 0.35 ± 0.05 Jy at 153 MHz and 0.14 ± 0.06 Jy at 325 MHz, which includes some flux contamination from the surrounding diffuse emission of source B.

In addition to the long tail, the 325 MHz map also contains a small tail of emission at the opposite side of source A. We must note that dynamic range limitations from calibration and imaging cause some artefacts near bright source A, therefore the apparently significant $> 15\sigma$ detection in the robust weighted 325 MHz map is more likely a $2 - 3\sigma$ detection when considering the local noise. If real, this detection could be related to the radio source just eastward of source A, which Miller, Owen & Hill (2003) associated with NGC 6331, although our detection extends $\sim 50''$ further east. This implies a spectral steepening of the small tail away from source A, which we cannot confirm in our spectral index map due to the non-detection at 153 MHz. It is tempting to associate the small tail with source A as well, which would provide source A with the typical double lobe morphology of a radio galaxy, with relativistic beaming being responsible for the contrast between the two lobes.

The low-frequency morphology of source B corresponds to the head-tail radio source observed at higher frequencies, with wide tail emission that (partly) merges north of the head into a single diffuse emission region. The view on the wide tail is confused by source A (and source A2, but for the discussion here we simply assume the narrow tail is part of source A). Assuming the emission from source A is confined to the bright emission areas, the tail of source B appears to extend beyond source A towards source C. This apparent connection is further supported by (i) the apparent continuity of the wide tail across source A in terms of flux level and boundary contours, (ii) the apparent presence of two tail extensions north of source A in the 153 MHz map, (iii) the steepening of the spectral index between source B and the apparent tail extension(s), and (iv) the extend of the tail in 1.4 GHz images (Röttgering et al. 1994; Clarke & Enßlin 2006), in which source A2 is not visible. If the diffuse emission north of source A is indeed part of the tail of source B, the total length of the tail is $\gtrsim 4'$, which corresponds to a projected length of $\gtrsim 270$ kpc, similar to the ~ 280 kpc length of NGC 1265 (Feretti et al. 1996) and over half the length of the long head-tail galaxy source C. The tail is slightly bend and widens from 1' at the head to $\sim 2.5'$ at the tail end.

There are two regions of emission for which we discuss alternative origins. A region of faint emission lies at the end of the (assumed) tail of source B at $17^{\text{h}}03^{\text{m}}15^{\text{s}}$, $+78^{\circ}39'30''$, which connects to source C (in projection). Wide-angle tail sources like source B are known to have tails that fade towards the tail end, but a morphological connection to another source may be possible. Based on the total intensity maps alone it may seem that some of the faint emission extends southwards from source C, but this is inconsistent with the required large velocity (relative to the intra-cluster medium, or ICM) of the galaxy found in the head source C to create the extremely straight, narrow-tail morphology (Röttgering et al. 1994). There is

no known cluster galaxy in the catalogs by Fabricant, Kent, & Kurtz (1989), Berrington, Lluguer & Cohn (2002) or Miller, Owen & Hill (2003) that lies in this area and generates this emission. In the absence of plausible alternatives, we assume that the low frequency tail of source B extends all the way up to source C.

The second region for which the origin is unclear is the bright emission region that appears to be connected to the western end of the wide tail of source B at $17^{\text{h}}02^{\text{m}}50^{\text{s}}$, $+78^{\circ}39'00''$, which we will call source B2. The dimensions of this region are approximately $1.2' \times 0.7'$, which corresponds to 80×47 kpc 2 at the mean cluster distance. The total flux estimates for source B2 at 153 and 325 MHz are 0.27 ± 0.05 Jy and 0.12 ± 0.01 Jy, respectively, which yields a spectral index estimate of -1.08 ± 0.36 between 153–325 MHz. From the catalog of Berrington, Lluguer & Cohn (2002) we identify a nearby cluster galaxy on the southern edge of source B2, namely J170248.9+783829.6. If this galaxy is responsible for the bright emission region, it must have ceased its radio activity, as there is no detection of radio emission from this source in the deep maps at 1.4 GHz (Röttgering et al. 1994; Miller, Owen & Hill 2003). The apparent alignment of source B2 with the tail from source A before the bend could indicate a physical relation, but this would require the narrow tail to be either unrelated to source A or to be displaced over a significant distance.

3.5. Source F

Source F has been noticed for its peculiar Z-shape and ultra-steep spectrum (e.g., Masson & Mayer 1978; Bridle et al. 1979). Based on the morphology at 1.4 GHz, source F was divided into three parts: the central bright region F2, the emission region F3 north-east of F2 and the faint emission region F1 south-west of F2. At 1.4 GHz, the region F3 has the appearance of a head-tail radio source (Röttgering et al. 1994), with an optical counterpart at the eastern head at redshift $z = 0.0563$ (Miller, Owen & Hill 2003) and considerable steepening of the spectrum from the head towards the tail end (-0.7 to -1.9) near source F2. Source F1 also resembles a head-tail source with spectral steepening along the tail (-1 to -1.6, ending at source F2) but at much fainter flux levels and without an optical counterpart at the head.

The emission of source F2 could be connected to both F1 and F3, but its true origin is unclear. In the absence of an optical counterpart for source F2, it has been speculated that sources F1, F2 and F3 are all part of the same source (Bridle et al. 1979), originating from the head of source F1. High resolution 1.4 GHz imaging reveals filamentary structure inside source F2 (Röttgering et al. 1994; Miller, Owen & Hill 2003), which has been noted to bear resemblance to the cluster relic source in Abell 85 at J004127-092300 (e.g., Slee et al. 2001). If source F2 resides at the mean cluster distance, the $1.4' \times 0.8'$ dimensions correspond to a proper size of 94×54 kpc 2 . The spectral index of source F2 between 350 MHz and 1.4 GHz is estimated at -1.71 ± 0.08 (Brentjens 2008).

Magnifications of the source F region from the GMRT 153 and 325 MHz maps are presented in Figure 6. Similar to Section 3.3, we estimate the flux of the source F components at 153 and 325 MHz by drawing image contours around their areas and summing the flux within. The resulting flux determination of source F1 is very uncertain, therefore

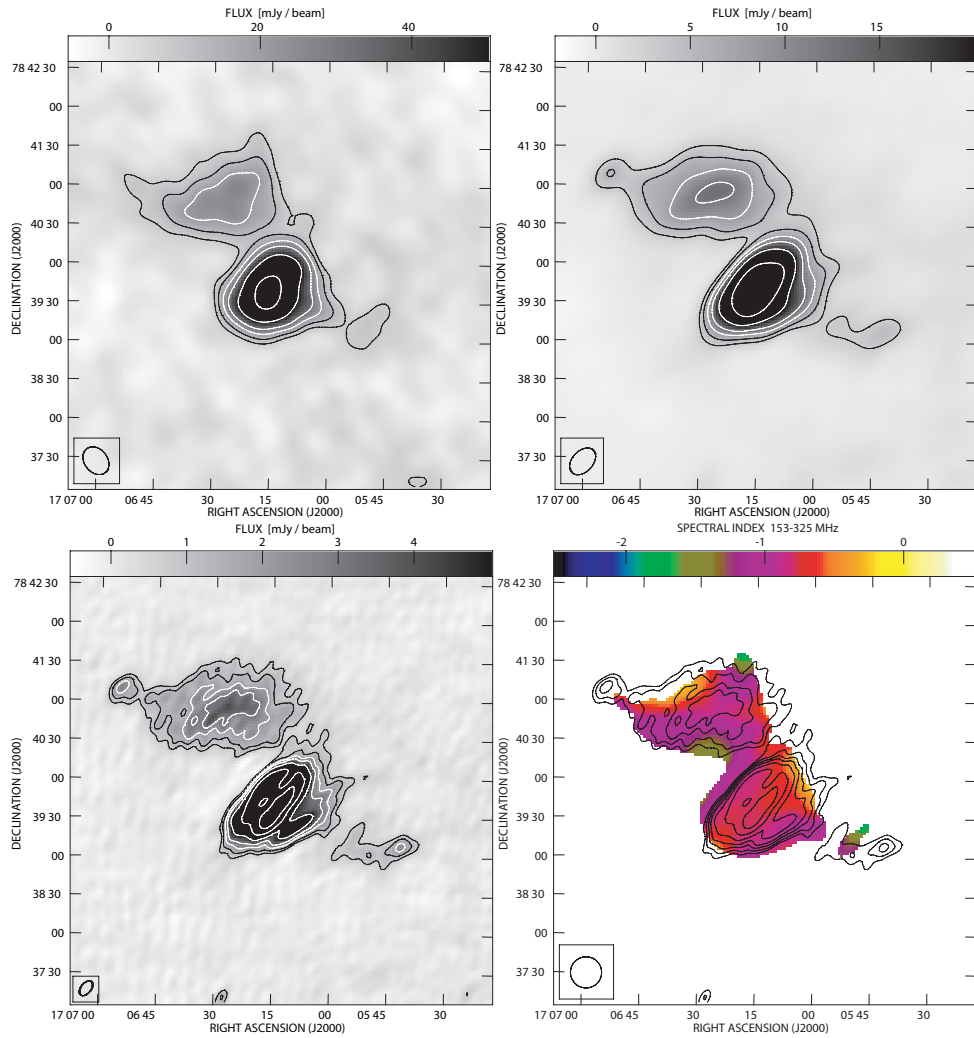


Figure 6: Detailed maps of the complex source F in A2256, similar to Figure 5. *Top Left:* Magnification of the GMRT 153 MHz map. Contours are drawn at $[4, 6, 10, 15, 24, 42, 72, 120, 240] \times$ the background RMS. *Top Right:* Magnification of the robust weighted GMRT 325 MHz map. Contours are drawn at $[15, 25, 40, 60, 100, 180, 300, 500, 1000] \times$ the background RMS. *Bottom Left:* Uniform weighted map of the GMRT 325 MHz. Contours are drawn at $[6, 10, 16, 25, 42, 75, 125, 210, 420] \times$ the background RMS. *Bottom Right:* Spectral index map from the GMRT 153 and 325 MHz maps. Contours are taken from the uniform weighted map.

omitted. For source F2, we find fluxes of 0.53 ± 0.02 Jy at 153 MHz and 0.30 ± 0.01 at 325 MHz, and for source F3 we find 0.18 ± 0.02 Jy at 153 MHz and 0.13 ± 0.01 at 325 MHz. The specified uncertainties do not include systematic uncertainties in the absolute flux scale. The 325 MHz flux of source F2 is a good match to the 325 MHz flux estimate of 0.29 ± 0.07 from the power-law model between 350 MHz and 1.4 GHz by Brentjens (2008). Our flux measurements at 325 MHz are significantly higher than the 327 MHz fluxes of 0.250 ± 0.018 Jy for source F2 and 0.078 ± 0.010 Jy for source F3 by Röttgering et al. (1994). While both maps have similar resolution, our background RMS is a factor ~ 2 lower. A visual comparison of the relic area in both maps clearly shows that our map is more sensitive to large-scale emission. These differences lead us to conclude that our 325 MHz flux measurements include a diffuse component that is not detected in the 327 MHz map by Röttgering et al. (1994). Our flux measurement of source F2 at 153 MHz is lower than the 151 MHz estimate of 0.65 Jy (no error

estimate quoted) by Bridle et al. (1979), but their estimate is based on differencing a low-resolution map against an extrapolated map from higher frequencies, which includes many assumptions and uncertainties. When adding a 20 percent uncertainty to this estimate, both measurements agree within error bars.

From the total flux measurements we find that the spectral index between 153–325 MHz is -0.76 ± 0.09 for source F2 and -0.43 ± 0.15 for source F3. Figure 6 also contains a spectral index map of the source F region over the same frequency range. There is a good match between the spectral index map of source F2 and the spectral index of -0.76 based on the total fluxes. For source F3, the spectral map is on average much steeper than -0.43, which indicates that the total flux measurement of source F3 includes a component at 325 MHz that is not detected at 153 MHz. Most likely, the 325 MHz measurement includes a diffuse component not seen at 153 MHz due to differences in sensitivity and UV-coverage, which becomes more impor-

tant for fainter sources like source F3. Except for the tail of source B, the regions in the spectral maps we discussed sofar are all regions with strong emission at 150 MHz. The combined spectral index results for source F2 from Brentjens (2008) and this work implies a large spectral index change from -0.76 between 153–327 MHz to -1.71 between 327 MHz and 1.4 GHz.

4. Discussion

Cluster mergers are known to have an effect on the appearance of radio sources in the cluster. Using the low-frequency observations from WSRT and GMRT we have presented a complementary radio view on several remarkable sources in A2256. The low frequency imaging yielded several interesting results that we discuss in this section.

4.1. A Radio Phoenix in the Cluster Periphery

Source F2 is located at the western edge of the radio halo, which coincides with the edge of the X-ray emission (e.g., Clarke & Enßlin 2006; Sun et al. 2002). In the nomenclature of Kempner et al. (2004), its steep spectrum, apparent size, apparent detachment from its origin qualifies source F2 as either a *radio phoenix* or an *AGN relic*, depending on whether or not the ICM has compressed the region to revive the radio emission. Given the geometry of source F, it seems reasonable to assume source F2 originates from the AGN associated with source F3, or possibly with an AGN previously associated with source F1. Reasons for assuming that source F2 is a radio phoenix that has been revived by a shock wave from the ICM are (i) the extreme steepening of the spectrum towards higher frequencies, (ii) its relative brightness, and (iii) the shell-like filamentary structure. Through semi-analytical modeling of compression of fossil radio plasma, Enßlin & Gopal-Krishna (2001) showed that compression of a radio cocoon with a steepened spectrum of aged synchrotron emission results in a flux enhancement while preserving the steep spectrum. Furthermore, numerical magneto-hydrodynamical (MHD) simulations by Enßlin & Brüggen (2002) showed that adiabatic shock compression of radio cocoons can produce radio sources with a shell-like filamentary appearance.

With the help of the synchrotron aging/revival model of Enßlin & Gopal-Krishna (2001) we investigate two scenarios for the origin of source F2: (1) the AGN relic scenario, in which the synchrotron emitting volume is aged but not shocked, and (2) the radio phoenix scenario, in which the aged synchrotron volume is adiabatically compressed by a (cluster merger) shock wave. The model includes many assumptions, therefore the outcome should be interpreted as an order of magnitude estimation. We adopt most of the model parameter values from the ‘smoking gun’ scenario by Enßlin & Gopal-Krishna (2001), as this describes the evolution of a small synchrotron emitting volume in the cluster periphery. Two important model input parameters are the current (observed) synchrotron volume and the magnetic field strength. For source F2 we adopted a cylindrical volume of $V = \pi d^2 l / 4 \approx 2 \cdot 10^{-4} \text{ Mpc}^3$, where we used the projected dimensions $l \times d = 94 \times 54 \text{ kpc}^2$ from Section 3.5. Using the revised minimum energy formulae by Beck &

Krause (2005)⁹, we estimated the magnetic field strength in source F2. From our flux measurement at 153 MHz, and assuming an injection spectral index of $\alpha = -0.7$, we derive a total magnetic field strength $B \sim 6 \mu\text{G}$, which is similar to the estimates by Brentjens (2008).

In scenario 1, an AGN that was active for $\sim 0.015 \text{ Gyr}$ is assumed to have injected relativistic electrons with an energy spectrum $N(E) \propto E^{2\alpha-1}$ into a volume V_0 , permeated with a magnetic field B_0 . After the AGN ceases activity, the volume expands further due to an over-pressure in the volume as compared to the surrounding gas at the cluster boundary. While expanding, the radio luminosity drops. Pressure equilibrium is reached on a time scale on the order of $\sim 0.01 \text{ Gyr}$. We used the model to calculate the visible spectrum during the volume expansion after the AGN activity ceased. Similar to Kale & Dwarakanath (2009), we manually varied the compression factor $C = V_0/V$ and the expansion time Δt_1 to obtain a good fit for the spectrum, normalized to the GMRT 153 MHz flux measurement $S_{153} = 0.53 \text{ Jy}$, as well as a good reproduction of the observed volume and magnetic field strength. Our fit included the GMRT 153 MHz and 325 MHz flux measurements, as well as the compiled flux points by Brentjens et al. (2008), but we excluded the rather uncertain 151 MHz estimate from Bridle et al. (1979). The best fit is given by $C = 0.23$ and $\Delta t_1 = 24 \text{ Myr}$, which implies $V_0 = 5 \cdot 10^{-5} \text{ Mpc}^3$, $B_0 = 16 \mu\text{G}$ and an initial 153 MHz flux of $S_{153} = 8.3 \text{ Jy}$.

In scenario 2, we continue the ‘smoking gun’ scenario by assuming pressure equilibrium is reached after $\Delta t_1 = 32 \text{ Myr}$. The initial volume has expanded by a factor of ~ 5 and is slowly loosing energy through synchrotron radiation over a period of $\Delta t_2 = 100 \text{ Myr}$. During the next $\Delta t_3 = 130 \text{ Myr}$, the volume is adiabatically compressed by a shock wave, reducing the volume to less than its initial size. The post-shock volume is again in pressure equilibrium with its environment, and continues to loose energy through synchrotron radiation. Similar to scenario 1, we manually varied the compression factor C and the spectral aging time Δt_4 after compression to obtain a good fit for the spectrum, observed volume and magnetic field strength. The best fit is given by $C = 3.2$ and $\Delta t_4 = 20 \text{ Myr}$, which implies $V_0 = 7 \cdot 10^{-4} \text{ Mpc}^3$, $B_0 = 2.8 \mu\text{G}$ and an initial 153 MHz flux of $S_{153} = 0.12 \text{ Jy}$.

Figure 7 shows plots of the model spectra for both scenarios. In both cases, our GMRT 325 MHz flux measurement lies significantly above the fitted curve. There was no parameter combination for which the 325 MHz measurement could be fitted accurately in combination with the 153 MHz and 1.4 GHz measurements. The models are consistent with all other measurements, given the uncertainties.

Due to the volume expansion, the AGN relic scenario requires an initial volume that is larger than the observed volume, while the initial magnetic field strength is requires to be stronger than the observed value. Furthermore, this scenario puts a rather strict time constraint on the age of the volume since the AGN turned off. For the radio phoenix scenario the requirements are less strict, because they do not only depend on age since the AGN turned off, but also on the time and strength of the shock compression. If, like assumed above, the compression factor is larger than one,

⁹ We made use of the BFIELD code version 10feb2006, available through the same authors.

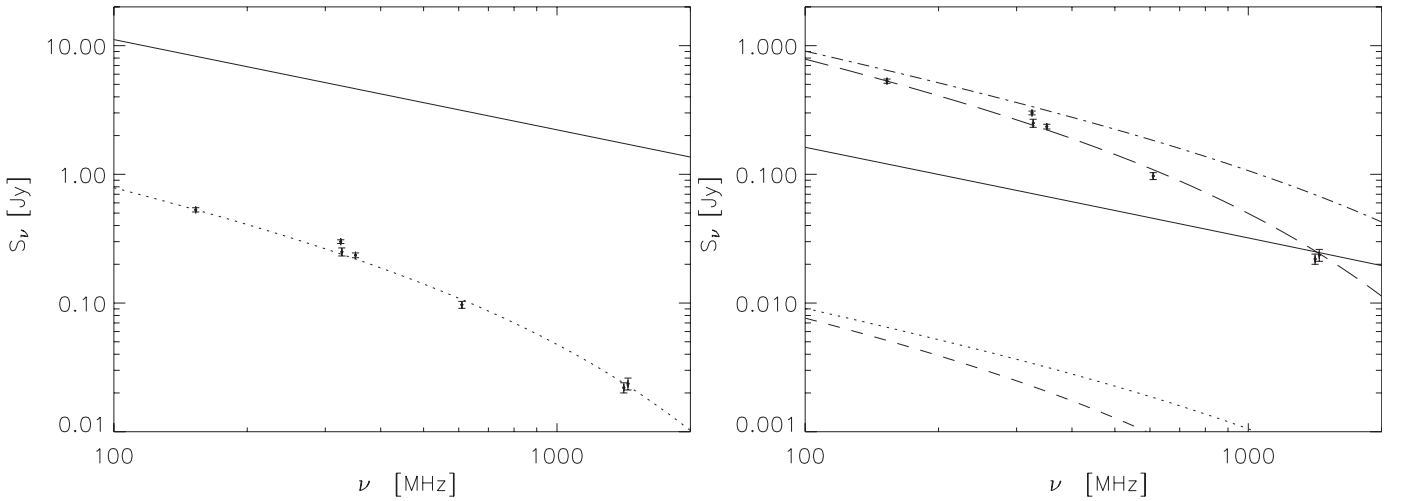


Figure 7: Fits of the synchrotron aging/revival model of Enßlin & Gopal-Krishna (2001) to the GMRT 153 MHz and 325 MHz flux measurements of source F2, complemented with the compilated flux points by Brentjens et al. (2008). *Left:* Scenario 1, in which the injected synchrotron emitting volume (solid line) ages to become an AGN relic (dotted line) before reaching pressure balance with its environment. *Right:* Scenario 2, in which the injected synchrotron emission (solid line) reaches pressure balance (dotted line), continues to loose energy through radiation (dashed line), gets adiabatically compressed (dot-dash line), and again continues to loose energy through radiation (long dashed line). See the text for more information.

the initial volume is larger than the observed volume, and the magnetic field strength is initially smaller.

For the following discussion, we assume that our model and the derived initial conditions are reasonably accurate. The magnetic field strength in galaxy clusters is typically found to be in the order of 0.5–5 μG , depending on the location in the cluster and the method and assumptions used for determining the magnetic field strength (Carilli & Taylor 2002 and references therein). A required initial field strength of 16 μG for the AGN relic scenario is therefore more excessive than the 2.8 μG for the radio phoenix scenario. Also, based on radio number counts (e.g., Intema et al. 2009c), an AGN with an initial 153 MHz flux of 8.3 Jy indicates a more rare type of source than the rather common 0.12 Jy for the radio phoenix. When considering an age of 24 Myr for the AGN relic, this requires the AGN to be present in the near vicinity. Taking the velocity dispersion of 1350 km s⁻¹ (Faber & Dressler 1977) as a typical velocity value, the angular displacement of the AGN galaxy in the sky plane is $\lesssim 25''$. Based on the age requirement, there is no discrepancy if source F2 is physically associated with source F3, but a physical association between source F1 and source F3 would be unlikely. Alternatively, there may be another, yet unidentified, galaxy involved. The less strict age requirement for the radio phoenix allows for many more options for the originating AGN galaxy.

Although not conclusive, the combined evidence presented here and in literature favours an explanation in which source F2 is a radio phoenix rather than an AGN relic. Revival of aged, steep-spectrum synchrotron emission through merger shock compression may be one of the mechanisms that is causing the detectable presence of this and several other steep-spectrum radio sources, as it can ‘simultaneously wake’ the fossil radio lobes that have been created in relatively short (~ 0.01 Gyr) AGN lifetimes and have been accumulating over a much longer (few Gyr)

(sub-)cluster lifetime. This can also explain the appearance of the newly discovered filamentary structures outside the halo/relic area by Van Weeren et al. (*in preparation*).

4.2. A Radio Phoenix at the Cluster Center?

The bright emission region near source A and B that we named source B2 is similar to source F2 in terms of angular size, shape, relative brightness and unknown origin, but differs in other observed properties: it is located (in projection) near the brightest of three X-ray peaks, the centers of possible merging subclusters that form the larger A2256 cluster (Sun et al. 2002), its 153–325 MHz spectrum is steeper, and there are no clear filamentary structures visible (but this could be a resolution issue). Source B2 also qualifies as an AGN relic or radio phoenix, for much of the same reasons as source F2. The indirect evidence for shock compression comes from the cluster merger scenario that has been proposed for A2256, based on radio and X-ray observations (Sun et al. 2002; Clarke & Enßlin 2006).

To extend the measured spectrum of source B2 to three points, we make an estimate of the 1.4 GHz flux by defining a rectangular area of $1.2' \times 0.7'$ and using the average between the first and second contour (225 $\mu\text{Jy beam}^{-1}$ for a $17.3'' \times 13.7''$ beam) in the map by Röttgering et al. (1994) as the mean flux level. Assuming a 25 percent uncertainty, this yields 3.7 ± 0.9 mJy. The spectral index between 325 MHz and 1.4 GHz is -2.3 ± 0.2 . Recalling the spectral index estimate of -1.08 ± 0.36 between 153–325 MHz (Section 3.4), this implies a large spectral steepening towards high frequency, similar to source F2.

Similar to source F2, we use the synchrotron aging/revival model of Enßlin & Gopal-Krishna (2001) to investigate the origin of source B2. We adopt most of the model parameter values from the ‘cocoon at the cluster center’ scenario. We assume a cylindrical volume of

$V = \pi d^2 l / 4 \approx 1.4 \cdot 10^{-4}$ Mpc³ (using the projected dimensions $l \times d = 80 \times 47$ kpc² from Section 3.4), and a total magnetic field strength $B \sim 6 \mu\text{G}$ from the revised minimum energy formulae by Beck & Krause (2005), assuming an injection spectral index of $\alpha = -0.7$. For scenario 1 (AGN relic), we obtain the best model fit in the phase where the unshocked volume is in pressure equilibrium with the surrounding gas, with $C = 0.60$ and $\Delta t_2 = 105$ Myr, which implies $V_0 = 8 \cdot 10^{-5}$ Mpc³, $B_0 = 8.5 \mu\text{G}$ and an initial 153 MHz flux of $S_{153} = 1.1$ Jy. For scenario 2 (radio phoenix), we obtain the best model fit for the phase in which the shocked volume is in pressure equilibrium with the surrounding gas, with $C = 3.8$ and $\Delta t_4 = 105$ Myr, which implies $V_0 = 5 \cdot 10^{-4}$ Mpc³, $B_0 = 2.5 \mu\text{G}$ and an initial 153 MHz flux of $S_{153} = 57$ mJy. The model fits and the flux measurements are plotted in Figure 8. Given that the spectra were scaled to the 153 MHz measurement, it was not possible to find model parameters that would create an accurate fit to both the 325 MHz and 1.4 GHz flux measurements. Similar to Section 4.1, this could be resolved if the 325 MHz flux was scaled down, but there are too few data points to be conclusive about the origin of this apparent discrepancy.

Similar to source F2, the requirements on the initial conditions of source B2 are more strict for the AGN relic scenario than for the radio phoenix scenario, but less extreme. In the AGN relic scenario, the total age (expansion plus equilibrium) $\Delta t_1 + \Delta t_2 = 5.4 + 105 \approx 110$ Myr would provide a galaxy displacement radius of $\lesssim 100''$. Alternatively, if source B2 is part of the tail of source B, the question rises why source B2 is much brighter than the rest of the tail. If it is shocked, why not the rest of the tail? The alignment and correspondance in brightness of source B2 with source A may indicate a physical relation, but we cannot proceed beyond speculation.

4.3. Bend Head-Tail Galaxies at the Cluster Center

If the low-frequency tail that we named source A2 is physically related to source A, it may belong to a class of bend head-tail galaxies in clusters, like 3C 129 in 4U 0446+44 (Miley 1973) and 4C 21.05 in Abell 84 (Giovannini & Feretti 2000). Mao et al. (2009) found that 5 head-tail galaxies in the merging A3125/A3128 supercluster live in regions of very high galaxy density (> 100 Mpc⁻³) in the vicinity of peaks in the X-ray emission. They argue that the radial peculiar velocities of their head-tail galaxies with respect to the supercluster average are too low to cause the bends in the tails, therefore winds in the ICM ('cluster weather') must be responsible. We compare the radial velocities of sources A and B (the latter also appears to have a slightly bend tail) against the A2256 cluster velocity distribution. Miller, Owen & Hill (2003) found $cz = 17565 \pm 54$ km s⁻¹ and 16417 ± 39 km s⁻¹ for sources A and B, respectively, and quote a systematic velocity of $cz_0 = 17490 \pm 74$ km s⁻¹ and a dispersion $\sigma_{cz} = 1269^{+56}_{-49}$ km s⁻¹. The peculiar velocity / dispersion ratios of sources A and B are +0.06 and -0.85, respectively, indicating that neither of both has a particularly large velocity along the line-of sight.

The very low peculiar velocity, combined with the possible double lobe morphology, suggests that source A is nearly at rest compared to the cluster center. This implies that the

bend in the low-frequency tail is indeed the result of bulk movement of the ICM, which could result from the cluster merger. Wide angle tail (WAT) sources like source B are also found to appear mainly in cluster merger scenarios (e.g., Sakelliou & Merrifield 2000). The negative velocity as compared to the cluster center, combined with the approximate north-south orientation of the tail, suggests that source B may have passed closer to the cluster center, i.e. closer to source A. Any displacement of ICM may have affected the tail of source B as well.

5. Summary

We have presented deep, low frequency radio observations of the galaxy cluster Abell 2256. In deep WSRT observations at 115–165 MHz we clearly detect the diffuse halo and relic emission, and measure a 140 MHz flux of 7.0 ± 0.9 Jy for the whole cluster. The mean spectral indices over the same frequency range for the relic and halo are estimated at ~ -1.2 and ~ -2 , respectively. We suggest that the flatter halo spectral index of -1.6 found by Brentjens (2008) can be the result of an over-estimation of invisible halo flux at 350 MHz and 1.4 GHz, the inaccuracy of several older flux measurements below 300 MHz, or a spectral flattening of the halo towards the southern and eastern boundary.

We used complementary deep GMRT observations at 153 and 325 MHz to study the regions containing sources A & B and the complex source F. We detected a tail of low frequency emission (which we named source A2) that appears to connect to the tail of source A at higher frequencies, which implies a (projected) bend of ~ 80 degrees. In the same area, we detected a emission region (named source B2) that has no clear origin. We speculated on the possible connection with either source A or B. Similar to source F2, source B2 also has no clear origin. The results of applying semi-analytical models for synchrotron aging/revival (Enßlin & Gopal-Krishna 2001) to the available flux measurements of source F2 favour a scenario in which source F2 is revived by shock compression. The outcome for source B2 is less clear.

The presence of revived synchrotron emission regions and bend head-tail sources are indicators of cluster merger activity (e.g., Enßlin & Gopal-Krishna 2001; Klamer, Subrahmanyam & Hunstead 2004; Mao et al. 2009). Although not conclusive, the results presented in this article support the hypothesis that the ICM of A2256 is disturbed by recent merger activity (e.g., Clarke & Enßlin 2006; Brentjens 2008).

Acknowledgements. The authors would like to thank both the staff of the WSRT and GMRT that made these observations possible. The WSRT is operated by the Netherlands Foundation for Research in Astronomy (ASTRON) with support from the Netherlands Foundation for Scientific Research (NWO). The GMRT is run by the National Centre for Radio Astrophysics (NCRA) of the Tata Institute of Fundamental Research (TIFR). HTI acknowledges a grant from the Netherlands Research School for Astronomy (NOVA).

References

- Beck, R. & Krause, M., 2005, Astron. Nachr., 326, 414
- Berrington, R.C., Lugger, P.M., & Cohn, H.N., 2002, AJ, 123, 2261
- Brentjens, M.A., & De Bruyn, A.G., 2004, in Proceedings of 'The Riddle of Cooling Flows in Galaxies and Clusters of Galaxies', Eds. Reiprich, T.H., Kempner, J.C. & Soker, N., p. 7
- Brentjens, M.A., 2008, A&A, 489, 69

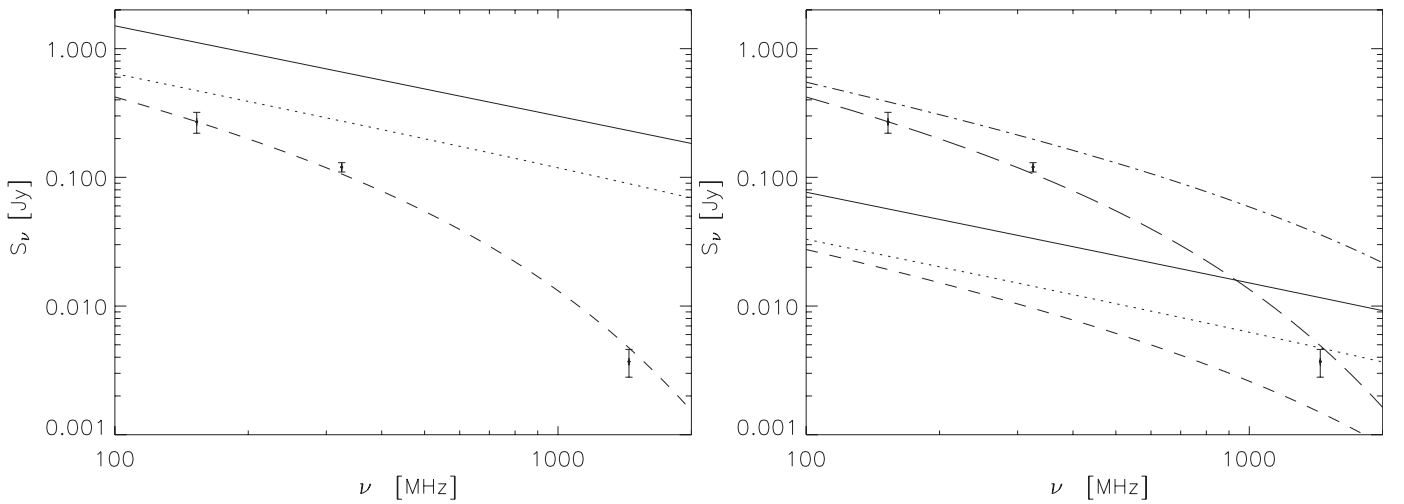


Figure 8: Fits of the synchrotron aging/revival model of Enßlin & Gopal-Krishna (2001) to the GMRT 153 MHz and 325 MHz flux measurements of source B2, complemented with a 1.4 GHz flux estimate using the map from Röttgering et al. (1994). *Left:* Scenario 1, in which the injected synchrotron emission (solid line) reaches pressure balance (dotted line) and continues to loose energy through radiation (dashed line). *Right:* Scenario 2, in which the injected synchrotron emission (solid line) reaches pressure balance (dotted line), continues to loose energy through radiation (dashed line), gets adiabatically compressed (dot-dash line), and again continues to loose energy through radiation (long dashed line). See the text for more information.

- Bridle, A.H., & Fomalont, E.B., 1976, A&A, 52, 107
 Bridle, A.H., et al., 1979, A&A, 80, 201
 Bridle, A.H. & Greisen, E.W., 1994, AIPS Memo 87
 Briel, U.G., et al., 1991, A&A, 246, L10
 Briggs, D.S., 1995, PhD Thesis, New Mexico Institute of Mining Technology, Socorro, New Mexico, USA
 Carilli, C.L., & Taylor, G.B., 2002, ARA&A, 40, 319
 Clarke, T.E., & Enßlin, T.A., 2006, AJ, 131, 2900
 Cohen, A.S., et al., 2007, ApJ, 134, 1245
 Condon, J.J., et al., 1994, ASPC, 61, 155
 Condon, J.J., et al., 1998, AJ, 115, 1693
 Cornwell, T.J., and Perley, R.A., 1992, A&A, 261, 353
 Cornwell, T.J., Braun, R. & Briggs, D.S., 1999, ASPC, 180, 151
 Costain, C.H., Bridle, A.H., & Feldman, P.A., 1972, ApJ, 175, L15
 Cotton, W.D., 1999, ASPC, 180, 357
 Cotton, W.D., et al., 2004, SPIE, 5489, 180
 Enßlin, T.A., & Gopal-Krishna, 2001, A&A, 366, 26
 Enßlin, T.A., & Brüggen, M., 2002, MNRAS, 331, 1011
 Faber, S.M., & Dressler, A., 1977, AJ, 82, 187
 Fabricant, D.G., Kent, S.M. & Kurtz, M.J., 1989, ApJ, 336, 77
 Feretti, L., et al., 1996, in ‘Extragalactic Radio Sources’, Proceedings of the IAU 175th Symposium, Eds. Ekers, R.D, Fanti, C. & Padrielli, L., p. 347
 Feretti, L., & Johnston-Hollitt, M., 2004, New A Rev., 48, 1145
 Giovannini, G. & Feretti, L., 2000, New A, 5, 335
 Hales, S.E.G., Baldwin, J.E., & Warner, P.J., 1988, MNRAS, 234, 919
 Hanisch, R.J., 1982, A&A, 116, 137
 Intema, H.T., 2009, arxiv:0904.3975, accepted for publication in A&A
 Intema, H.T., 2009, *in preparation*
 Intema, H.T., 2009, *in preparation*
 Jaffe, W.J., & Perola, G.C., 1973, aap, 26, 423
 Kettenis, M., et al., 2006, ASPC, 351, 497
 Lonsdale, C.J., 2005, ASPC, 345, 399
 Kale, R., & Dwarakanath, K.S., 2009, arXiv:0905.0966, accepted for publication in ApJ
 Kempner, J.C., & Sarazin, C.L., 2001, ApJ, 548, 639
 Kempner, J.C., et al., 2004, in Proceedings of ‘The Riddle of Cooling Flows in Galaxies and Clusters of Galaxies’, Eds. Reiprich, T.H., Kempner, J.C. & Soker, N., p. 335
 Klamer, I., Subrahmanyam, R., & Hunstead, R.W., 2004, MNRAS, 351, 101
 Komatsu, E., et al., 2009, ApJS, 180, 330
 Mao, M.Y., et al., 2009, MNRAS, 392, 1070
 Masson, C.R., & Mayer, C.J., MNRAS, 185, 607
 Miley, G. K., 1973, A&A, 26, 413
 Miley, G.K., 1980, ARA&A, 18, 165
 Miller, N.A., Owen, F.A., & Hill, J.M., 2003, AJ, 125, 2393
 Noordam, J.E., 2004, SPIE, 5489, 817
 Perley, R.A., 1989, ASPC, 6, 259
 Rengelink, R.R., et al., 1997, A&AS, 124, 259
 Röttgering, H.J.A., et al., 1994, ApJ, 436, 654
 Röttgering, H.J.A., et al., 1997, MNRAS, 290, 577
 Sakelliou, I., & Merrifield, M.R., 2000, MNRAS, 311, 649
 Schwab, F.R., 1984, AJ, 89, 1076
 Slee, O.B., et al., 2001, AJ, 122, 1172
 Sun, M., et al., 2002, ApJ, 565, 867